Interactional Structural Loads of the XV-15 Rotor in Airplane Mode

Joon W. Lim
U.S. Army Combat Capabilities Development Command Aviation & Missile Center
Aviation Development Directorate
Ames Research Center, Moffett Field, CA

Steven Tran
Science & Technology Corp.
Ames Research Center, Moffett Field, CA

ABSTRACT

An investigation of the rotor/airframe interactions of the XV-15 tiltrotor aircraft in airplane mode is conducted using high fidelity CFD. To separate the rotor installation effects, an isolated rotor and a half-span full aircraft are simulated at the cruise speeds of 160 and 220 knots. The installed rotor displays a doublet aerodynamic loading near the 270^o azimuth along with low-frequency mode harmonic airloads in the first half of the cycle. The doublet aerodynamic loading is due to the interactions with the wing and the low-frequency harmonic airloads are due to the rotor dynamics and longitudinal cyclic pitch control. The installed rotor thrust and power display significant 3/rev loading that is typical for a three-bladed rotor. More importantly, the resulting low-frequency mode harmonic airloads trigger vibrations on the rotor as a forcing function. The installed rotor displays significant installation effects on the 2 to 4/rev harmonics of the blade torsional, flap, and lead-lag moments at 220 knots.

NOTATION

M^2c_c	Non-dimensional chord force, positive towards the leading edge
M^2c_m	Non-dimensional pitching moment
M^2c_n	Non-dimensional normal force
R	Rotor radius, 150 inches
U_P	Blade section normal velocity, positive down through the rotor disk, ft/s
U_T	Blade section tangential velocity, positive against the rotor rotation, ft/s
ψ	Rotor azimuth angle, counter-clockwise rotation for the starboard rotor, zero degree azimuth at the top of the rotor in airplane mode, deg

INTRODUCTION

Tiltrotors are a versatile class of rotorcraft that combine the high speed capabilities of fixed wing vehicles with the vertical lift capabilities of conventional helicopters. Rotors and large engine nacelles with heavy motor drive/transmission components are mounted on a hefty thick wing. Thus, aerodynamic interactions associated with propulsion devices and airframe (e.g., the wings, fuselage, nacelle, and control surfaces) are complex in nature. Furthermore, the nature of the interactional aerodynamics of tiltrotor aircraft is significantly different for hover, transition, and cruise. In airplane mode, the nacelles are tilted forward and proprotor blades cut through flow field in front of the wing. The resulting flow field of the proprotor are influenced with the wing and the airframe, and thus displays unsteady loadings on the proprotor blades. Such interactional aerodynamic phenomena naturally translate into interactional vibrations, noises, and fatigue loads.

A number of investigations of tiltrotors aerodynamics in cruise have been made using CFD. Clark (Ref. 1) performed a numerical examination using a panel code VSAERO (Ref. 2) on the wing/rotor and rotor/rotor interference effects for a generic tiltrotor in hover and forward flight at advance ratio of 0.14.

Schillings and Reinesch (Ref. 3) addressed the significance of employing a CFD tool in predicting interactional aerodynamics for tiltrotor configurations. The paper compared the interactional flow field characteristics between the VSAERO result and the Bell Helicopter in-house aero-elastic analysis DYN5 (Ref. 4) result for the V-22 full-scale configuration at 313 knots. They also correlated the predicted n/rev bending moments with the 0.2-scale V-22 semi-span aeroelastic wind tunnel data at 100 knots. They concluded that the interactional aerodynamics triggered a 3/rev flap bending moment on the proprotor blade and that the VSAERO/C81 predicted the 3/rev bending moment well while the DYN5 had difficulty with accurate prediction.

McVeigh et al. (Ref. 5) investigated the interactions between the rotors and airframe for tiltrotors in hover, transition, and airplane mode using test data and analyses. They concluded that the rotor blade motion of moving up in the wing-

Presented to the 45th European Rotorcraft Forum, Warsaw, Poland, September 17-20, 2019.

inboard due to the counter-clockwise rotation increased the wing lift and reduced the wing drag in airplane mode.

Lim (Ref. 6) characterized the mechanism of the XV-15 (Ref. 7) rotor/wing interaction in airplane mode using the CFD solver, HPCMP CREATE™-AV HELIOS (Ref. 8). The wing thickness interference contributed to a single positive-peak impulsive loading while the wing loading interference contributed to a doublet loading. The wing interference increased the mean rotor thrust by 12.7% and the mean power by 8.1%. Note that the rotor was at the fixed collective and untrimmed and the blade was simulated as a rigid blade.

Tran et al. (Ref. 9) investigated the complex aerodynamic behaviors of tiltrotor during hover, conversion, and cruise using HELIOS. The CFD predictions were compared against the experimental data and GTR flight simulation data (Ref. 10). The HELIOS predictions showed that significant interactional effects occurred on the rotor during hover and cruise.

The present paper explores tiltrotor proprotor/wing interactions using HELIOS. The objective of this paper is to assess the interactional, aerodynamic and structural rotor loads due to the wing-to-rotor interference for the XV-15 (Fig. 1) tiltrotor in airplane mode.

Figure 1. XV-15 in airplane mode.

INTERACTION MECHANISMS

The weight of a tiltrotor aircraft is sustained primarily by the wing in airplane mode, and thus the lifting wing carries large circulations that interact with the rotor. When the rotating blades operate in close proximity to the wing in airplane mode, they are exposed to significant mutual rotor/wing aerodynamic interactions as illustrated in Fig. 2. When the blade cuts through the flow field in front of the wing (near 270° rotor azimuth), the aerodynamic angles of attack on the blade change due to

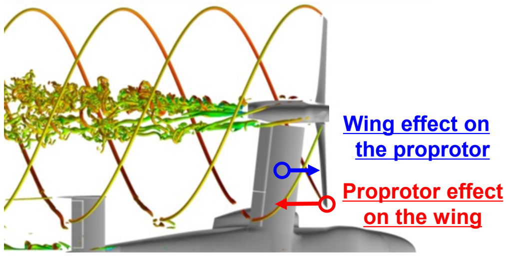

Figure 2. XV-15 Proprotor/wing aerodynamics interactions in tiltrotor airplane mode.

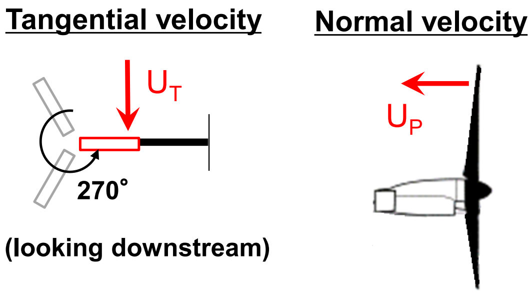

Figure 3. Blade sectional velocities of the installed proprotor on the wing. The section velocities are shown in a positive sign convention.

interactions with the wing. The angles of attack on the blade change by means of the perturbations of the normal (U_P) and tangential (U_T) velocities on the blade (see Fig. 3). These perturbation velocities are measured relative to the freestream velocity. U_P is defined positive down through the rotor disk and U_T is positive against the rotor rotation. Figure 4 illustrates a schematic of the individual interactional aerodynamics mechanisms of the installed proprotor on the lifting wing by means of U_P and U_T as the blade operates near 270° azimuth. The impacts on the proprotor velocities are illustrated by solid red arrows.

The XV-15 wing has a 23%-thick airfoil section as its primary source of aircraft lift. The wing thickness introduces a blockage effect on the slipstream ahead of the wing leading edge. After passing through the proprotor, the slipstream immediately encounters the wing structure that makes the flow field behind the proprotor slow down or become re-directed around the wing thickness. This is referred to as the “wing thickness effect.”

The wing thickness effect generates an effective upwash on the proprotor that yields a single up-peak normal velocity and a small doublet fluctuation (from positive to negative) of tangential velocity when a blade cuts in front of the wing

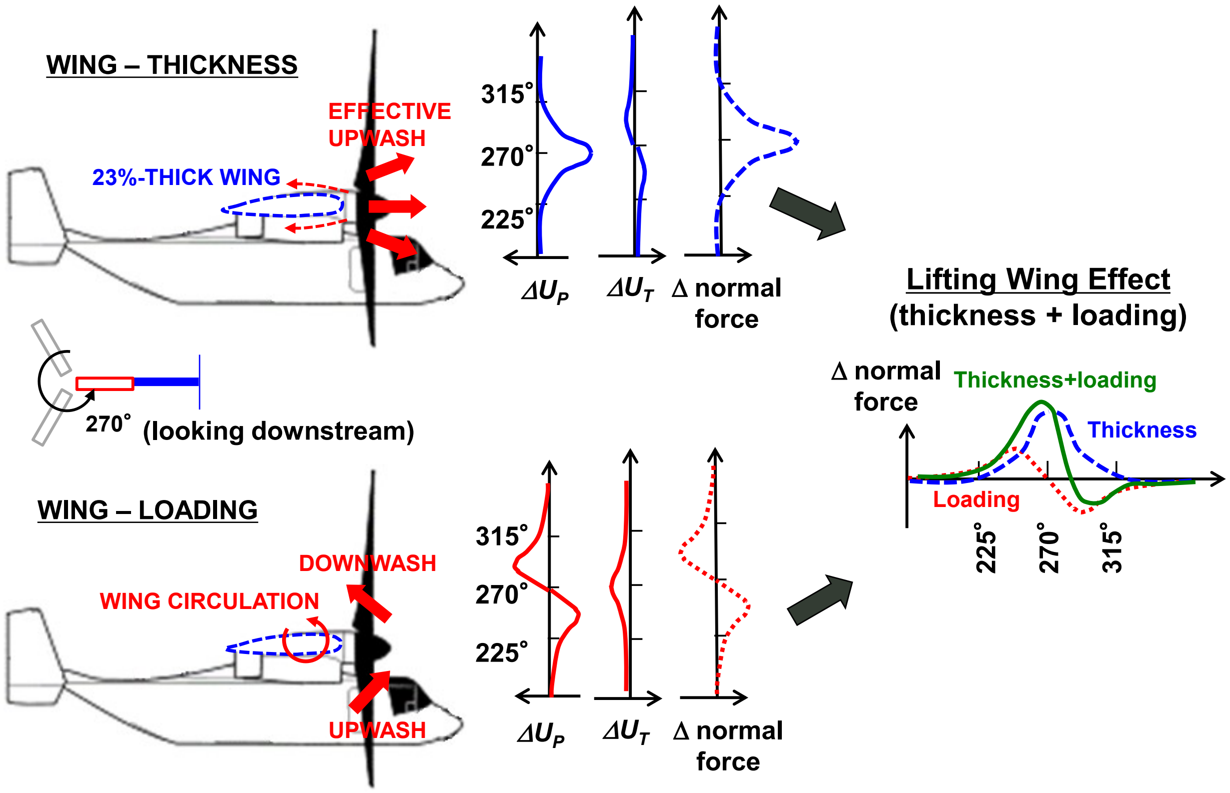

Figure 4. A schematic of the mechanism of the wing effects on the proprotor.

(azimuth of 270°). As a result, the perturbation normal force produces an impulsive up peak in front of the wing that occurs once per rotor revolution per blade. The doublet fluctuation of the perturbation tangential velocity is small compared to the tangential velocity so its contribution to the normal force is also small.

The wing circulation generates a doublet wash (i.e., an upwash followed by a downwash) on the perturbation normal velocity of the blade when the blade cuts in front of the wing. It also adds a small down peak to the perturbation tangential velocity but since the magnitude of the perturbation tangential velocity is relatively small, its contribution is negligible. Thus, the resulting normal force displays a doublet loading in front of the wing. This interaction is called the “wing loading effect.”

Overall the perturbation normal force due to both the wing thickness and wing loading effects displays a doublet loading with the effect of the wing thickness dominating.

COMPUTATIONAL METHODOLOGY

HELIOS v9, an overset CFD code based on a multi-mesh, multi-solver paradigm, is used in this study (Ref. 8). The unique infrastructure of the code allows for the modeling of complex geometries by leveraging the strengths of several CFD solvers in the regions directly surrounding the body. HELIOS is able to couple with multiple solvers including NASA’s OVERFLOW (Ref. 11) and FUN3D (Ref. 12) solvers and the native strand capability, mStrand (Ref. 13). In the far field regions, structured Cartesian grids are automatically generated and solved through the native SAMCart solver (Ref. 14).

HELIOS also has the ability to perform CFD/CSD coupling using RCAS (Ref. 15) which allows the blades to be trimmed throughout the course of simulations. RCAS is a comprehensive, multidisciplinary code used for the analysis of complex rotorcraft configurations. These analyses include trim and flight controls, aerodynamic and structural modeling, and aeroelastic stability.

For the proprotor blades, NASA’s fully structured overset solver OVERFLOW 2.2n is used. OVERFLOW discretizes the Navier-Stokes equations using finite difference schemes of up to 6th-order spatial accuracy for the convective fluxes and 2nd order for the viscous fluxes. The code is 2nd order accurate in time with an implicit dual time stepping method. In the present study, the fully-structured blade grids have 269x141x74 nodes and thus the resulting rotor grids including the cap grids

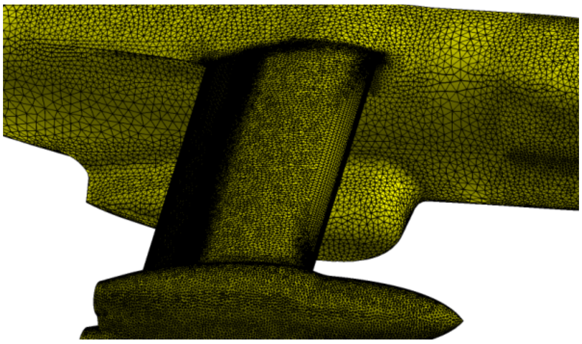

Figure 5. Part of surface grids over the main body of XV-15.

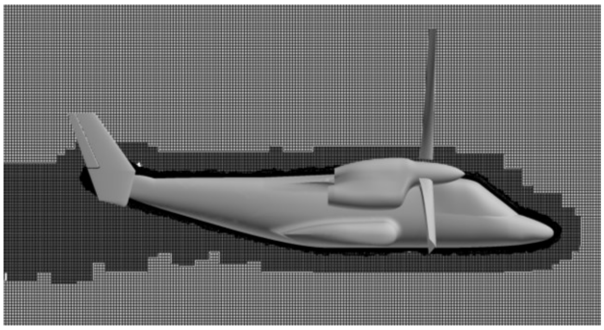

Figure 6. Structured off-body Cartesian grids surrounding the vehicle showing the fixed and adaptive mesh refinements. Every other point is shown.

have 12.1 million nodes in total. The outer boundary of the blade near-body grids is located approximately 1.2 chords (blade nominal chord) from the blade surface. The y+ grid spacing at the wall is less than 1.

The XV-15 fuselage is treated as a half-span model with a symmetry plane along the centerline. This was done in order to reduce the computational costs of the simulations. Due to the complexities of the fuselage geometry, unstructured grids are used for the fuselage with the FUN3D solver. FUN3D is an unstructured node-centered finite volume code with 2nd order accuracy in both space and time. In this study, the convective fluxes are computed using a Roe flux difference splitting scheme. The average cell spacing on the surface of the body is approximately 0.5 inches. The surface mesh is depicted in Fig. 5. In the volume, clustered boundary layer elements are grown from the surface with the first layer height such that y+ < 1. The fuselage grids have approximately 17.2 million nodes in total.

In the off-body region, the native SAMCart solver is used. SAMCart is a structured Cartesian solver based on a 5th order central difference scheme. For temporal discretization, it uses an implicit BDF2 solver. A fixed refinement region is imposed around the aircraft. This refinement region spans [-R, 5.25R] x [0, 3R] x [-2R, 2R] with a grid spacing of 0.10c where c is the chord of the proprotor. Adaptive solution-based mesh refinement is also used in order to track and selectively resolve the complex vortex dynamics which develop in the wake of the aircraft. The criteria used for adaption is GAMR (Ref. 16). For the adapted regions, the finest grid spacing is equal to 0.05c. An example of the adapted off-body grid is shown in Fig. 6. The off-body grids have 181 million nodes in total (without including the fringe points).

The simulations considered in this study are assumed to be fully turbulent and so the Spalart-Allmaras Detached Eddy Simulation (SA-DES) model is used throughout all of the solvers. These simulations were run until the forces on the vehicle bodies were converged. This typically took about 5 full rotor revolutions for cruise.

In this study, RCAS is loosely coupled to HELIOS in order to trim the rotor. The RCAS rotor model consists of eleven nonlinear beam elements per blade with a pitch link system for the structural model and eighteen segments per blade for the aerodynamic model. The pitch link pushrod is modeled with a slide element. The gimbal mounted at the rotor hub is simulated using a gimbal hinge element with a spring stiffness value based on a CAMRAD II XV-15 model used in the previous work (Ref. 17). To ensure numerical stability, an additional "trim damper" on the gimbal hinge that is only active during the trim analysis is introduced with the damper value based on the earlier RCAS study (Ref.18). The "trim damper" is active for the trim analysis and removed for the other analyses. Since the gimbal hinge is simulated by the universal joint type hinge with an additional damper, the predicted blade loads in the vicinity of the gimbal hinge may not be adequate for XV-15 rotor.

In order to separate the interactional effects on the rotor loads, two rotor simulation models are used – an isolated rotor and an installed rotor on the half-span aircraft (see Fig. 7). Note that the installed rotor model represents the starboard rotor.

DISCUSSION

Simulations are made for airplane mode at the cruising speeds of 160 and 220 knots. Zero deflection is set for the wing flap, flaperon, elevator and rudder. A 2-DOF trim strategy is employed for airplane mode. The proprotor collective and longitudinal cyclic pitch are trimmed in order to match the thrust (T, positive forward) and H force (drag, positive up) to the GTR data (Ref. 10). The aircraft attitudes are prescribed using the GTR data. Table 1 shows the values of rotor forces and power

Table 1. Proprotor rotor forces and power and blade response from the GTR data. Rotor operates at 517 RPM in the sea level.

Speed knots	Thrust lbs	H force lbs	Power hp	Pitch deg	Longitudinal flap deg
160	680.80	104.77	475.2	4.332	0.582
220	916.24	-94.01	812.1	0.687	1.742

and blade response from the GTR data. It is worth noting that the lateral flap angles are negligible within a tolerance range.

The XV-15 aircraft utilizes three-bladed, stiff-in-plane, gimbal-mounted rotors. The detailed aircraft geometry descriptions are provided in Table 2.

Table 2. Summary of the XV-15 aircraft.

Wing	
Airfoil	NACA 64A223
Span	386 in
Chord	63 in
Sweep	-6.5°
Dihedral	2°
Rotor	
Airfoil	NACA 64 series
Blade	3
Radius	150 in
Solidity	0.0891
Chord	14 in
Precone	2.5°
Twist	-45°

Rotor Natural Frequencies

The rotor natural frequencies indicate the vibration characteristics of an elastic rotor blade. Figure 8 shows a fan plot of the XV-15 rotor blade where RCAS frequencies are compared against the CAMRAD II results. The RCAS blade frequencies were calculated for the gimbal locked. The blade control is set at 0-degree collective *in vacuo* with the nominal rotor speed of 589 RPM.

The first torsion and the third flap frequencies display differences between RCAS and CAMRAD II.

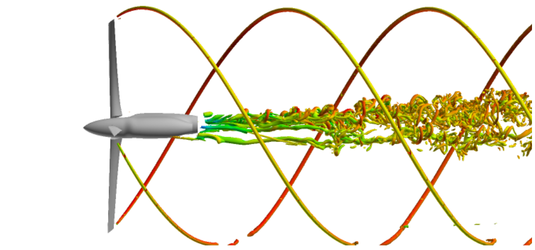

a) Isolated rotor

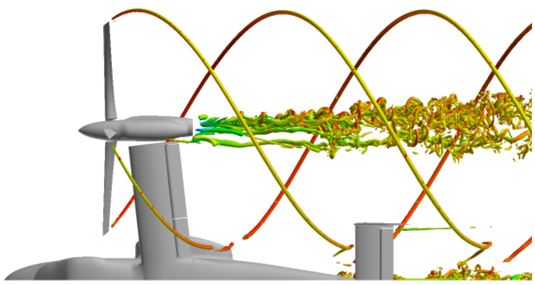

b) Installed rotor

Figure 7. The isolated and installed rotor simulation models.

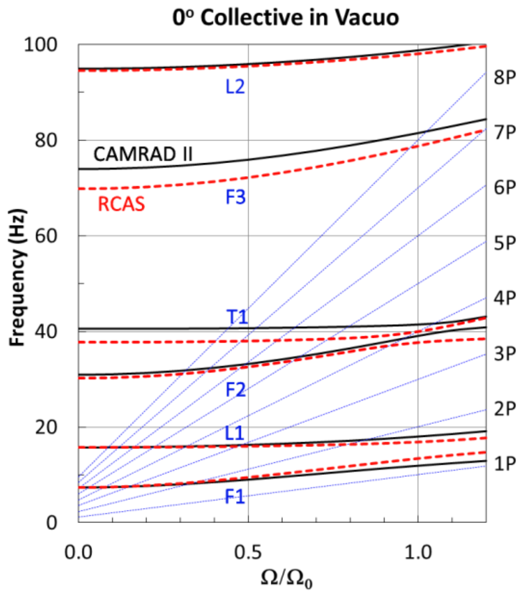

Figure 8. Comparison XV-15 rotor blade frequencies using RCAS and CAMRAD II. The blade collective is set 0 degrees. The rotor operates at 589 RPM in vacuo.

The first torsion frequency of RCAS is softer than the CAMRAD II frequency, which consequently influences the third flap frequency through the flap-torsion coupling. Because of this lower prediction of the torsion frequency, the frequency coalescence between the second flap and first torsion modes occurs at a lower RPM than the CAMRAD II. Overall, however, the frequencies reasonably agree between the two analyses.

Blade Airloads

When the proprotor blade cuts the flow field in front of the wing at 270° azimuth, the blade is exposed to strong interactions with the airframe. The primary interactions on the proprotor are due to the wing thickness and loading interferences. As discussed previously, the wing thickness effect produces a single up-peak impulsive loading and the wing loading effect generates a doublet loading. As stated in Ref. 6, the wing thickness effect was dominating.

Figure 9 compares the sectional airloads at r/R=0.87 for the isolated and installed rotors at the cruise speed of 160 knots. The elastic rotor with 2 DOF trim analysis was used. For both the isolated and installed rotors, a strong 1/rev load is seen from the non-dimensional sectional normal force (M^2c_n), chord force (M^2c_c), and pitching moment (M^2c_m), which results from the rotor longitudinal pitch control. The installed rotor displays a doublet loading near the 270° azimuth along with low-frequency harmonic loads in the first half of cycle. The doublet loading is caused by the interactions with the wing. The low-frequency harmonic loads in the first half of cycle are due to elastic rotor blade dynamics. It is worth noting that the waveform of the pitching moment of the installed rotor near the 270° azimuth appears more complex than just a doublet loading.

Figure 10 shows the same comparison of the sectional airloads but at 220 knots. The differences of the waveforms between the isolated and installed rotors become larger at 220 knots, which implies that the dynamics and interaction effects are stronger at 220 knots than at 160 knots.

Harmonic analysis results presented in Fig. 11 were obtained using FFT for the sectional airloads at 220 knots. The mean values of the installed sectional airloads are noted at the top of each of the plots. Since minimal differences in the means were found between the installed and isolated rotors, the mean values of the isolated rotor were omitted.

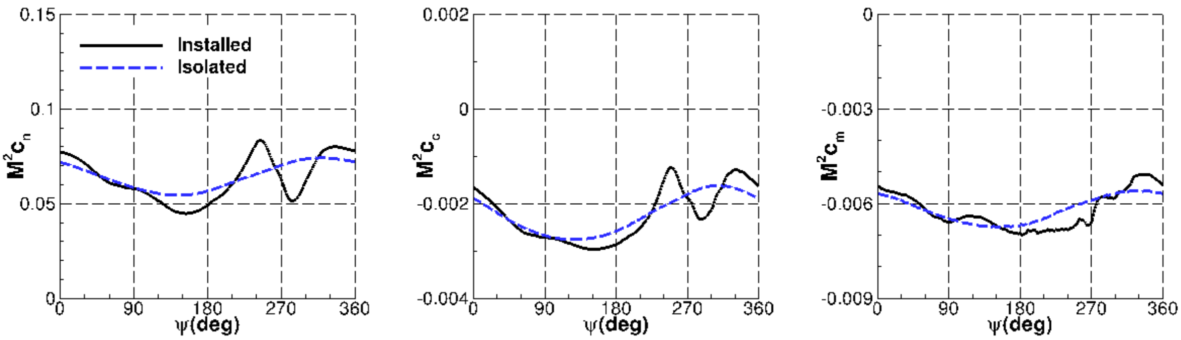

a) M^2c_n b) M^2c_c c) M^2c_m

Figure 9. Comparison of sectional airloads at r/R=0.87. Wind speed is 160 knots.

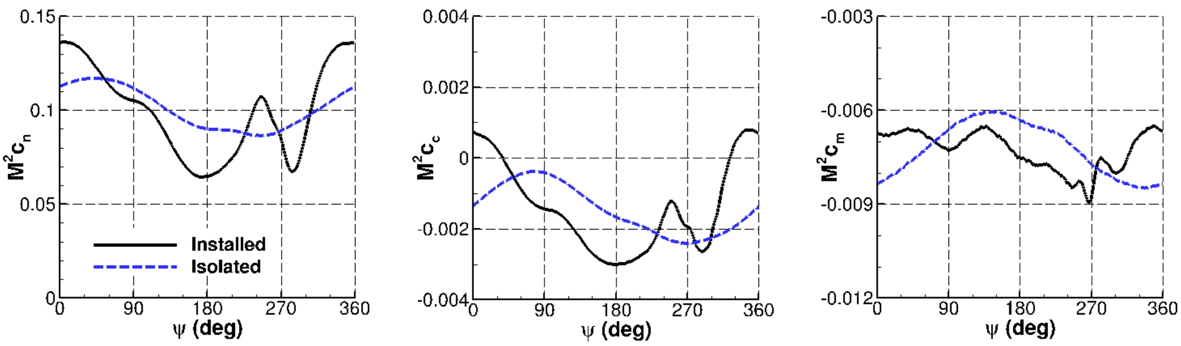

a) M^2c_n b) M^2c_c c) M^2c_m

Figure 10. Comparison of sectional airloads at r/R=0.87. Wind speed is 220 knots.

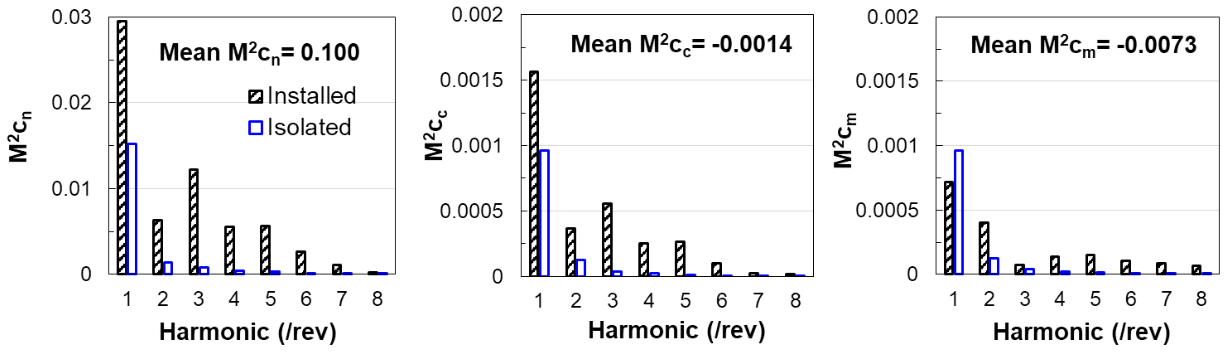

a) M^2c_n b) M^2c_c c) M^2c_m

Figure 11. Harmonic contents of blade sectional airloads at r/R=0.87. Wind speed is 220 knots.

Overall, the 1 to 6/rev harmonics of the installed rotor significantly larger compared to those of the isolated rotor, which is due to the dynamics and installation interference effects.

The contours of the sectional normal force (M^2c_n) are produced in Fig. 12-13 at the cruise speeds of 160 and 220 knots. The contours of the normal forces of the isolated and installed rotors and their delta difference when looking downstream are presented. The ΔM^2c_n values are calculated by subtracting the values of the isolated rotor from the installed rotor. The installation effects are found

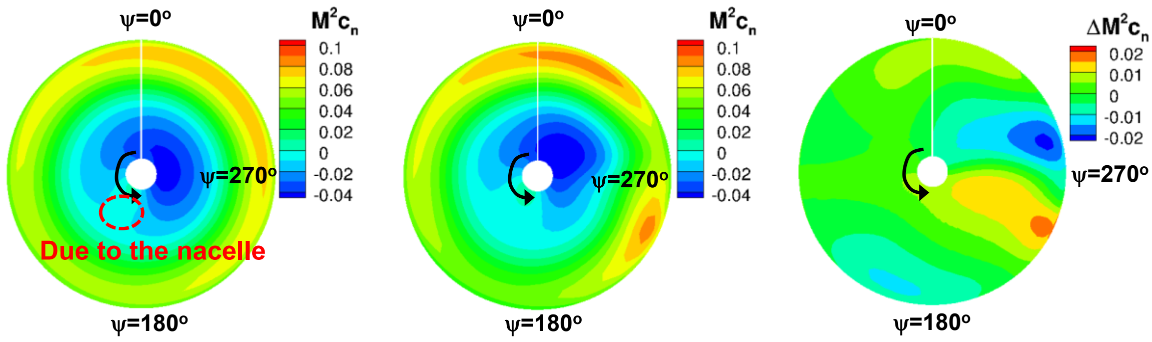

a) Isolated rotor b) Installed rotor c) Delta M^2c_n

Figure 12. Comparison of the blade sectional M^2c_n contours at r/R=0.87. Wind speed is 160 knots.

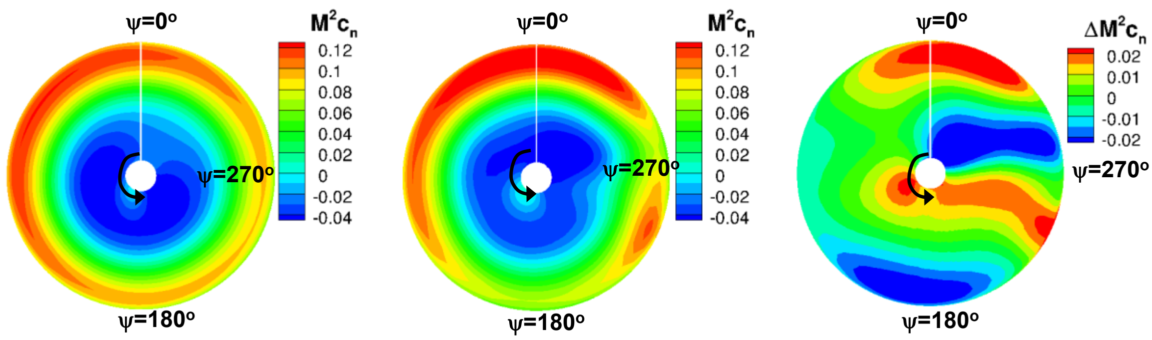

a) Isolated rotor b) Installed rotor c) Delta M^2c_n

Figure 13. Comparison of the blade sectional M^2c_n contours at r/R=0.87. Wind speed is 220 knots.

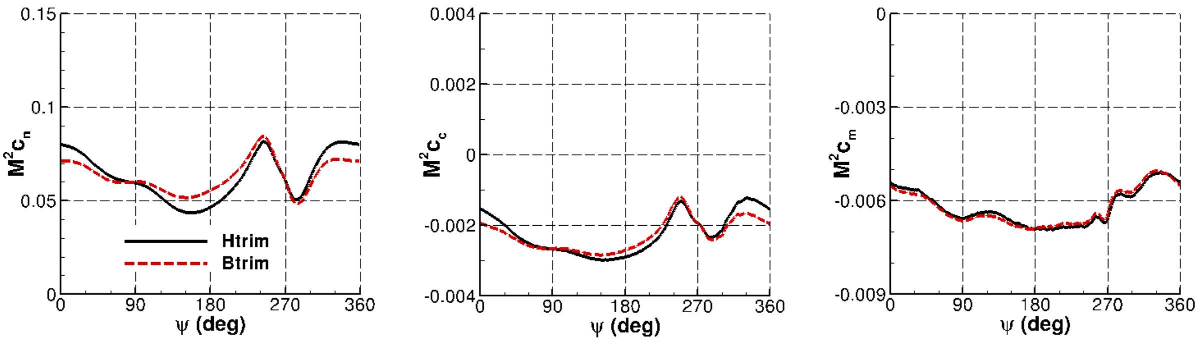

Figure 14. Comparison of the sectional airloads computed using the trim target of H force (Htrim) and longitudinal flapping response (Btrim) at r/R=0.87 for 160 knots.

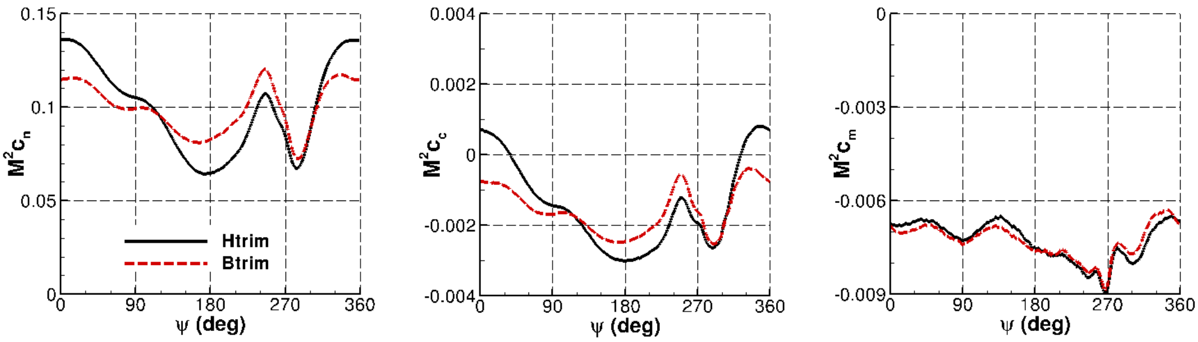

Figure 15. Comparison of the sectional airloads computed using the trim target of H force (Htrim) or longitudinal flapping response (Btrim) at r/R=0.87 for 220 knots.

most significant in the vicinity of the 270° azimuth with a band width of 60° to 90°. The broken axisymmetric pattern in the 2nd quarter (near the 170° azimuth) near the blade root is caused by the presence of the nacelle. It is interesting to observe strong 1/rev delta M^2c_n (the hot spot at the 0° azimuth and the cold spot at the 180° azimuth) especially for the 220 knots, which may be related to the trim strategy.

The trim targets used in the present study are rotor thrust and H force, which is labeled as Htrim. To understand the sensitivity of the 1/rev delta M^2c_n, a typical trim strategy is employed by taking rotor thrust and blade longitudinal flapping angle (Btrim) with the values in Table 1. The computed sectional airloads using these two trim analyses are compared in Figs. 14-15 for 160 and 220 knots, respectively. The waveforms of the two analyses show similar characteristics, but the 1/rev delta M^2c_n are larger with the Htrim case. Although the predicted M^2c_n could be exaggerated with the Htrim and smaller differences between the Htrim and Btrim cases would be favorable, these differences result from the differences in prediction capabilities of the GTR and Helios codes. Therefore, more efforts need to be made in the future for better understanding, and the Htrim case is consistently used in the following discussions.

The blades in close proximity of the wing display impulsive doublet sectional airloads when the blades cut the flow field in front of the wing. Integrating these sectional airloads over the blade span provides the integrated blade airloads. Summing the integrated blade airloads over the number of blades produces the rotor airloads. Figure 16 compares the rotor thrust and power at 160 and 220 knots. The installed rotor thrust and power display significant 3/rev loading as is typical for a three-bladed rotor. These 3/rev rotor loads will transmit to the rotor pylon resulting in vibrations in the airframe.

The effect of the wing on the rotor loads were investigated in Ref. [6] by comparing the rotor loads between the isolated and installed rotors, which showed that the wing interference raised the XV-15 rotor thrust by 12.5% and the rotor power by 8.0% at the cruise speed of 220 knots. However, these outcomes were obtained without performing a trim analysis. In the present study, the 2-DOF rotor trim

Table 3. Predicted mean rotor loads of the isolated and installed rotors at 220 knots.

	Thrust lbs	Power hp
Isolated	917.5	844.6
Installed	908.5	841.7
Delta loads (%)	1.0%	-0.3%

Table 4. Predicted 3/rev (amplitude) rotor loads of the isolated and installed rotors at 220 knots.

	3/rev Thrust lbs	3/rev Power hp
Isolated	30.9 (3%)	12.7 (2%)
Installed	288.8 (32%)	206.1 (24%)

* The percentages show a ratio to its own mean

strategy is employed so that the rotor thrust and H force are set to match the GTR data. The resulting mean thrust and power are compared in Table 3 for the isolated and installed rotors. The delta loads are defined as the difference between the isolated and installed loads. Since it is selected for trim target, the rotor thrust matches the GTR target within a tolerance range (10 lbs) for both the isolated and installed rotors. It is also found that the predicted power of the isolated and installed rotors are higher by 3.6-4.0% than the GTR target, but the difference between the two rotors is within a tolerance range, which implies that the installation effect on the mean rotor power is negligible.

The 3/rev rotor loads between the isolated and installed rotors are compared in Table 4. The installation effects influence the 3/rev loads significantly. Compared to the isolated rotor, the installed rotor produces significant 3/rev harmonic oscillations – 32% for the thrust and 24% for the power.

Blade Moments and Pitch Link Load

It was shown in Fig. 11 that the rotor/airframe interaction triggered the 1 to 6/rev harmonics of the blade sectional airloads. Consequently, these interacted harmonic airloads influence blade bending moments as a forcing function. Figure 17 shows the blade torsion, flap, and lead-lag moments at r/R=0.375 for a cruise speed of 220 knots. The torsional moment is defined positive leading edge up, the flap moment is positive flap down, and the lead-lag moment is positive in a lead motion. Similar to the sectional airload comparison, a 1/rev blade moment is dominant for the isolated rotor but more of the lower harmonic moments are produced for the installed rotor.

The blade moments at r/R=0.375 are analyzed using FFT. The resulting harmonic contents are compared in Fig. 18 for the isolated and installed rotors. For the isolated rotor, the 1 to 2/rev moments appear significant and other higher harmonic components seem relatively insignificant. The 1/rev moments are influenced mainly by the longitudinal cyclic pitch from the trim analysis. The 2/rev moments are caused primarily by the rotor dynamics that result from the blade elasticity and gimbal motions coupled with the interactions. The 3 to 5/rev moments display the installation effect, and the installation effect seems significant for the 3/rev moments.

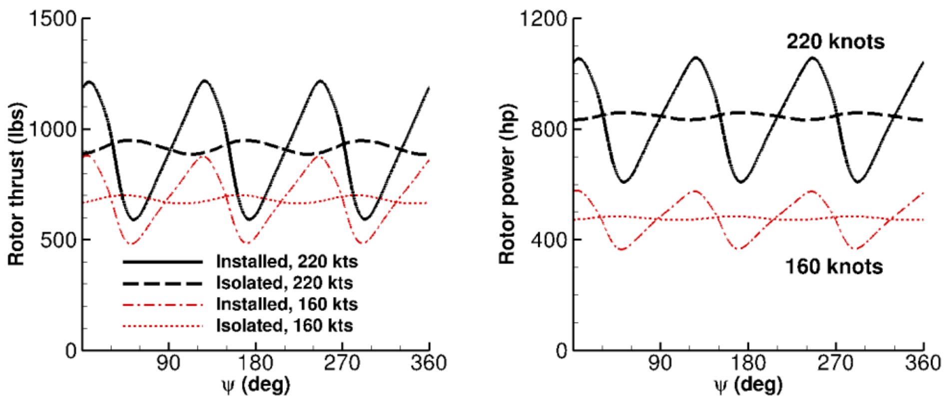

Figure 16. Comparison of rotor thrust and power between the isolated and installed rotors.

Figure 19 shows a full spectrum of the installation effects on the blade moments at the cruise speed of 220 knots. The comparisons are made along the blade span for the 1 to 5/rev harmonics of the blade torsional, flap, and lead-lag moments. Although the 1/rev moment is influenced more by the longitudinal cyclic pitch, the 2 to 4/rev moments show relatively large installation effects. A similar conclusion was drawn in Ref. 3 that the 2 to 4/rev harmonics of blade bending moments of the V-22 0.2-scaled model rotor resulted from the rotor/airframe interactions.

CONCLUDING REMARKS

An investigation of the rotor/airframe interactions of the XV-15 tiltrotor aircraft is conducted using high fidelity CFD for the cruise speeds of 160 and 220 knots. The focus is on the structural loads of the installed XV-15 rotor which results from the aerodynamic interferences with the airframe. The following conclusions are made:

- The installed rotor showed a doublet blade sectional airloads near the 270° azimuth due to the interactions with the wing. It also showed the low-frequency harmonic sectional airloads that were due to the rotor blade dynamics.
- The isolated and installed rotors showed a dominating 1/rev blade sectional load due to the longitudinal cyclic control trim.

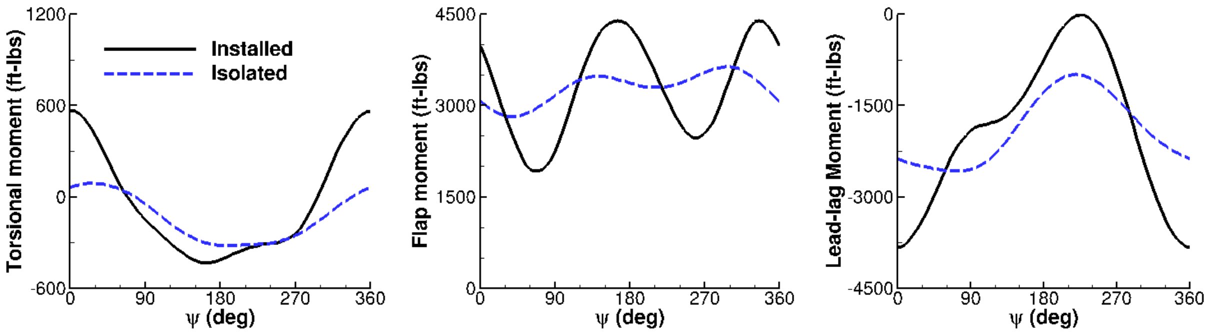

a) Torsional moment b) Flap moment c) Lead-lag moment

Figure 17. Comparison of blade moments at r/R=0.375 between the isolated and installed rotors. Wind speed is 220 knots.

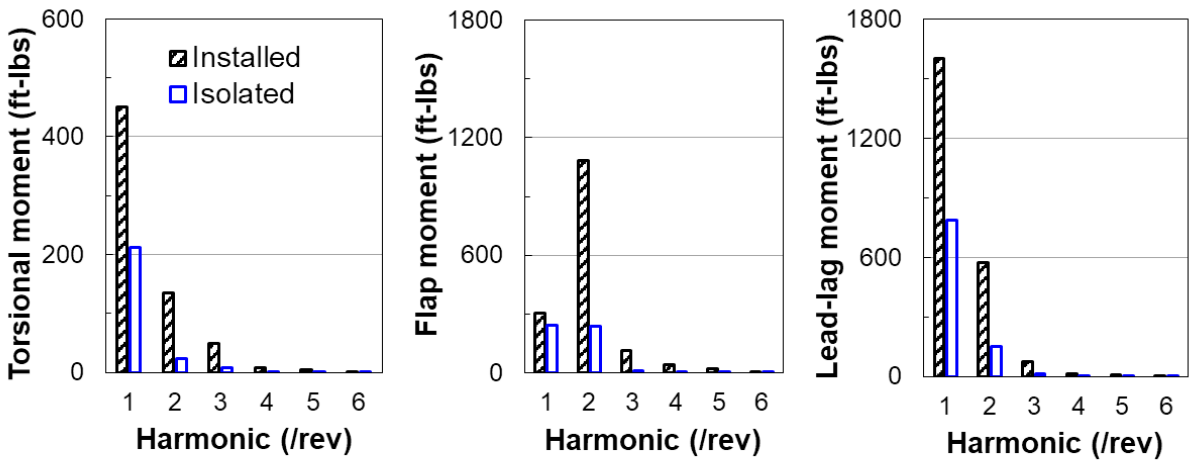

a) Torsional moment b) Flap moment c) Lead-lag moment

Figure 18. Harmonic contents of blade moments at r/R=0.375. Wind speed is 220 knots.

- The installed rotor thrust and power displayed significant 3/rev loading that is typical for a three-bladed rotor.

- Installation effects had a large impact on the higher harmonic behavior of the installed rotor. Significant 2 to 4/rev harmonics of the blade torsional, flap, and lead-lag moments were produced due to the installation effect.

ACKNOWLEDGMENTS

The authors would like to acknowledge Cecil W. Acree at NASA Ames Research Center for providing data on the XV-15 rotor. The author would like also

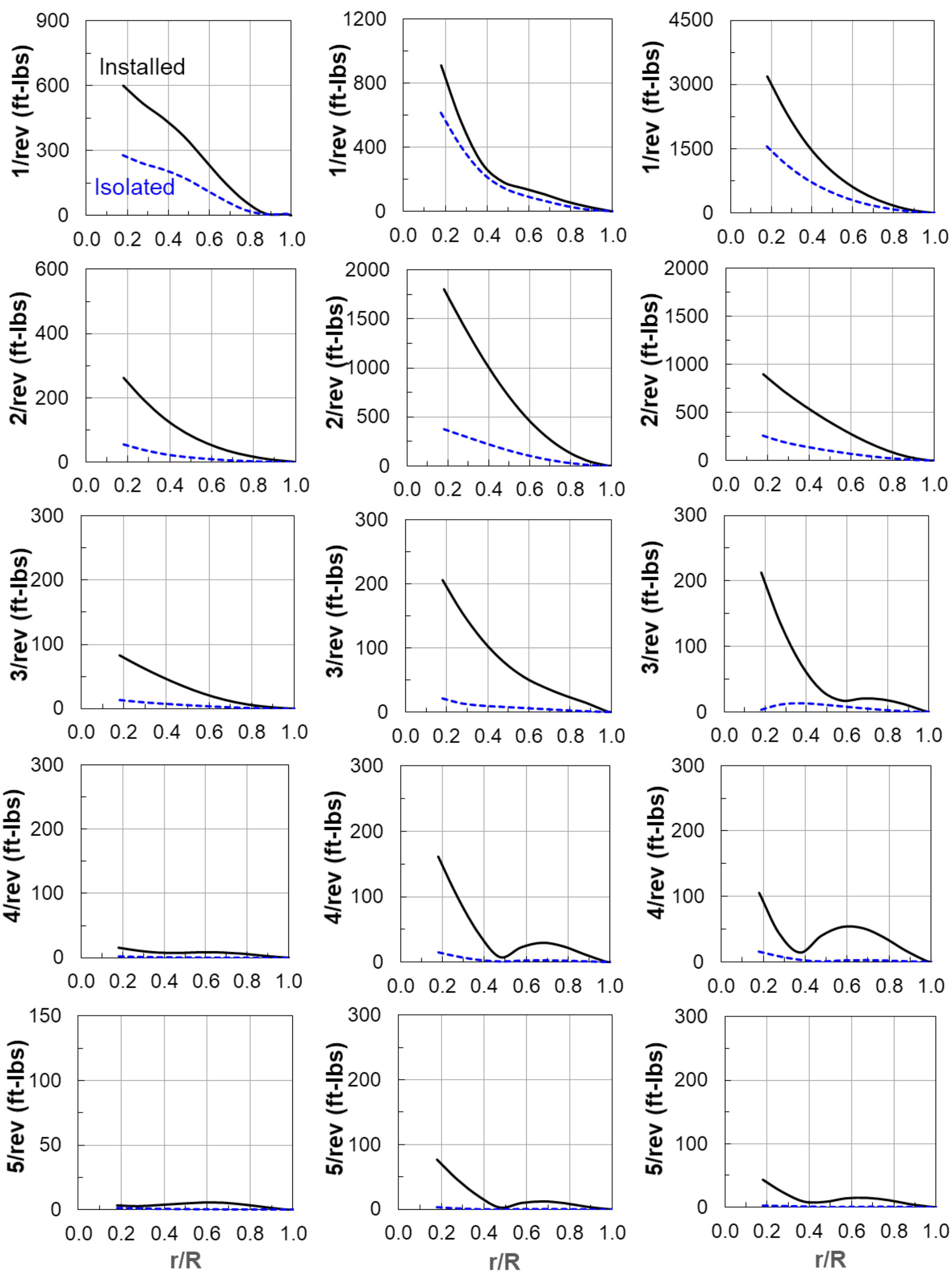

a) Torsional moment b) Flap moment c) Lead-lag moment

Figure 19. Harmonic contents of blade moments along the blade span. Wind speed is 220 knots.

to express many special thanks to Wayne Johnson, NASA Ames Research Center, for his invaluable insights, guidance, and encouragement on completion of this study. Material presented in this paper is a product of the HPCMP CREATE™-AV Element of the Computational Research and Engineering for Acquisition Tools and Environments (CREATE) Program sponsored by the U.S. Department of Defense HPC Modernization Program Office.

REFERENCES

[1] Clark, D. R., "Analysis of the Wing/Rotor and Rotor/Rotor Interactions Present in Tilt-Rotor Aircraft," *Vertica*, Vol. 11, No. 4 (1987), pp. 731-749.

[2] Maskew, B., "Prediction of Subsonic Aerodynamic Characteristics: A Case for Low-Order Panel Methods," *Journal of Aircraft*, Vol. 19, No. 2, February 1982, pp.157-163.

[3] Schillings, J. and Reinesch, R., "The Effect of Airframe Aerodynamics on V-22 Rotor Loads," *Journal of the American Helicopter Society*, Vol. 34, (1), January 1989, pp. 26-33.

[4] Yen, J. G., Weber, G. E., and Gaffey, T. M., "A Study of Folding Proprotor VTOL Aircraft Dynamics," Air Force Flight Dynamics Laboratory Technical Report 71-7, Vol. 1, September 1971.

[5] McVeigh, M. A, Grauer, W. K., and Paisley, D. J., "Rotor/Airframe Interactions on Tiltrotor Aircraft," Proceedings of the 44th American Helicopter Society Annual Forum, Washington, D. C., June 1988.

[6] Lim, J. W., "Fundamental Investigation of Proprotor and Wing Interactions in Tiltrotor Aircraft," Proceedings of the VFS 75th Annual Forum & Technology Display, Philadelphia, Pennsylvania, May 13–16, 2019.

[7] Maisel, M. D., "Tilt Rotor Research Aircraft Familiarization Document," NASA TM-X62, 407, Ames Research Center and U.S. Army Air Mobility R&D Laboratory, Moffett Field, CA, January 1975.

[8] Wissink, A., Staruk, W., Tran, S., Roget, B., Jayaraman, B., Sitaraman, J., and Lakshminarayan, V., "Overview of New Capabilities in HELIOS Version 9.0," Proceedings of AIAA SciTech 2019 Forum, San Diego, CA, January 7–11, 2019.

[9] Tran, S., Lim, J. W., Nunez, G., Wissink, A., and Bowen-Davies, G., "CFD Calculations of the XV-15 Tiltrotor During Transition," Proceedings of the VFS 75th Annual Forum & Technology Display, Philadelphia, Pennsylvania, May 13–16, 2019.

[10] Ferguson, S. W., "Development of a Simulation for Generic Tilt-Rotor Aircraft," NASA CR-166537, 1989.

[11] Nichols, R. H., and Buning, P. G., "User's Manual for OVERFLOW 2.2," NASA Langley Research Center, October 2017, overflow.larc.nasa.gov/home/users-manual-for-overflow-2-2/

[12] Biedron, R. T., Carlson, J., Derlaga, J. M., Gnoffo, P. A., Hammond, D. P., Jones, W. T., Kleb, B., Lee-Rausch, E. M., Nielsen, E. J., and Park, M. A., "FUN3D Manual: 13.3", 2018.

[13] Sitaraman, J., Lakshminarayan, V. K., Roget, B., and Wissink, A. M., "Progress in Strand Mesh Generation and Domain Connectivity for Dual-Mesh CFD simulations", Proceedings of the 55th AIAA Aerospace Sciences Meeting, 2017.

[14] Wissink, A., Sitaraman, J., Jayaraman, B., Roget, B., Lakshminarayan, V., Potsdam, M., Jain, R., Leffell, J., Forsythe, J. R., and Bauer, A., "Recent Advancements in HELIOS Rotorcraft Simulation Code", Proceedings of the 54th AIAA Aerospace Sciences Meeting, San Diego, CA, January 4–8, 2016.

[15] Saberi, H., Hasbun, M., Hong, J., Yeo, H., and Ormiston, R. A., "Overview of RCAS Capabilities, Validations, and Rotorcraft Applications", American Helicopter Society 71st Annual Forum, Virginia Beach, VA, May 5-7, 2015.

[16] Kamkar, S. J., Wissink, A. M., Sankaran, V., Jameson, A., "Feature-Driven Cartesian Adaptive Mesh Refinement for Vortex-Dominated Flows", Journal of Computational Physics, Vol. 230, No. 16, July 2011, pp. 6271-6298.

[17] Acree, C. W., Peyran, R. J., and Johnson, W., "Rotor Design Options for Improving XV-15 Whirl-Flutter Stability Margins," NASA/TP-2004-212262, March 2004.

[18] Corle, E., Floros, M., and Schmitz, S., "Transient CFD/CSD Tiltrotor Stability Analysis," Proceedings of the AIAA SciTech 2019 Forum, 7-11 January 2019, San Diego, California.

The authors confirm that they, and/or their company or organization, hold copyright on all of the original material included in this paper. The authors also confirm that they have obtained permission, from the copyright holder of any third party material included in this paper, to publish it as part of their paper. The authors confirm that they give permission, or have obtained permission from the copyright holder of this paper, for the publication and distribution of this paper as part of the ERF proceedings or as individual offprints from the proceedings and for inclusion in a freely accessible web-based repository.